Cooperative shear in bulk metallic glass composites containing metastable β-Ti dendrites

Zhang, L.; Narayan, R. L.; Sun, B. A.; Yan, T. Y.; Ramamurty, Upadrasta; Eckert, J.; Zhang, H. F.

2020

Zhang, L., Narayan, R. L., Sun, B. A., Yan, T. Y., Ramamurty, U., Eckert, J., & Zhang, H. F. (2020). Cooperative shear in bulk metallic glass composites containing metastable β-Ti dendrites. Physical Review Letters, 125(5), 055501-. doi:10.1103/physrevlett.125.055501

https://hdl.handle.net/10356/145778

https://doi.org/10.1103/PhysRevLett.125.055501

Cooperative Shear in Bulk Metallic Glass Composites Containing Metastable β-Ti Dendrites

L. Zhang,[1] R. L. Narayan,[2] B. A. Sun,[3] T. Y. Yan,[1] U. Ramamurty,[4] J. Eckert,[5,6] and H. F. Zhang[1,*]
[1]*Institute of Metal Research, Chinese Academy of Sciences, Shenyang 110016, China*
[2]*Department of Materials Science and Technology, Indian Institute of Technology Delhi, Delhi 110016, India*
[3]*Institute of Physics, Chinese Academy of Sciences, Beijing 100190, China*
[4]*Department of Mechanical and Aerospace Engineering in Nanyang Technological University, Singapore 637331, Singapore*
[5]*Erich Schmid Institute of Materials Science, Austrian Academy of Sciences, A-8700 Leoben, Austria*
[6]*Department of Materials Science, Chair of Materials Physics, Montanuniversität Leoben, A-8700 Leoben, Austria*

(Received 11 April 2020; accepted 22 June 2020; published 28 July 2020)

We report a novel plastic deformation mechanism of bulk metallic glass composites (BMGCs) containing metastable β-Ti dendrites. Plastic deformation of the BMGCs beyond the ultimate tensile strength is mediated by cooperative shear events, which comprise a shear band in the glassy matrix and a continuous ω-Ti band with a thickness of ~10 nm in the β-Ti dendrite. The cooperative shear leads to serrated shear avalanches. The formation of narrow ω-Ti bands is caused by high local strain rates during the cooperative shear. The cooperative shear mechanism enriches the deformation mechanisms of BMGCs and also deepens the understanding of ω-Ti formation.

DOI: 10.1103/PhysRevLett.125.055501

Shear banding is the main mechanism dominating plastic deformation of bulk metallic glasses (BMGs) [1]. Under constrained loading conditions, such as bending or compression, BMGs generally deform through a sequence of discrete slips, known as serrated or jerky flow, at room temperature [1,2]. A serration event is accomplished by fast nucleation and propagation, known as shear avalanche, together with the arrest of a shear band [3,4]. A shear band forms by cooperative shear of nanometer-scaled shear transformation zones (STZs) [5], and it is a highly localized deformation band with a thickness of ~10 nm [1,2]. The dynamics of serrated flow in BMGs have been intensively studied [3,4,6,7], and the cumulative distribution of shear-avalanche sizes follows a universal power-law relation multiplied by an exponentially decaying scaling function as depicted by the mean-field theory [6,8]. In comparison, under uniaxial tension, BMGs exhibit zero plasticity due to the fast runaway of a detrimental shear band [2,9].

In order to improve the tensile plasticity of BMGs, bulk metallic glass composites (BMGCs) containing *in situ* formed crystals during solidification [10] have been developed. Zr/Ti-based BMGCs containing β-Zr/Ti phases [10–13] and CuZr-based BMGCs containing $B2$ CuZr phases [14,15] are two most intensively investigated kinds of BMGCs. However, the macroscopic serrated flow manner of BMGCs under tension normally disappears, because the shear bands are well restricted in the intercrystalline glassy regions [16]. BMGCs often exhibit strain softening, because hardening caused by dislocation entanglement in the crystals cannot sufficiently compensate shear softening in the glassy matrix [11,12]. Recent research has shown that this drawback can be overcome and strain hardening can be obtained via incorporating deformation-induced phase transformations or twinning of the metastable crystals [14,17].

In this Letter we report a novel plastic deformation mechanism of BMGCs containing metastable β-Ti dendrites under tension. Beyond the ultimate tensile strength (UTS), the BMGCs undergo macroscopic serrated flow, and the plastic deformation is mediated by cooperative shear events, which comprise a shear band in the glassy matrix and an ω-Ti band in the β-Ti dendrite. The statistics of the shear avalanches and the formation mechanism of narrow ω-Ti bands are also analyzed.

An alloy with a nominal composition of $Ti_{45.7}Zr_{33}Cu_{5.8}Co_3Be_{12.5}$ (at. %) was prepared by arc melting a mixture of pure metals (purities ≥99.9%) in a Ti-gettered high-purity argon atmosphere. The alloy was remelted five times to ensure chemical homogeneity, followed by casting the melt into ϕ14 mm rods in a copper mold. Samples cut from the as-cast rods and the tension-fractured samples were characterized by means of x-ray diffraction (XRD; Philips PW 1050, Cu K_α), scanning electron microscopy (SEM; Zeiss Supra 55) combined with energy-dispersive x-ray spectroscopy (EDS), and transmission electron microscopy (TEM, FEI Titan G3) with probe and image Cs correctors. TEM specimens were ion milled using a Gatan 695 device. Flat dog-bone shaped tensile specimens with gauge dimensions of 14 mm × 2 mm × 0.8 mm were cut from the as-cast rods as per the ASTM standard E8M [18]. The quasistatic tension tests were carried out on an Instron 5582 machine at an initial

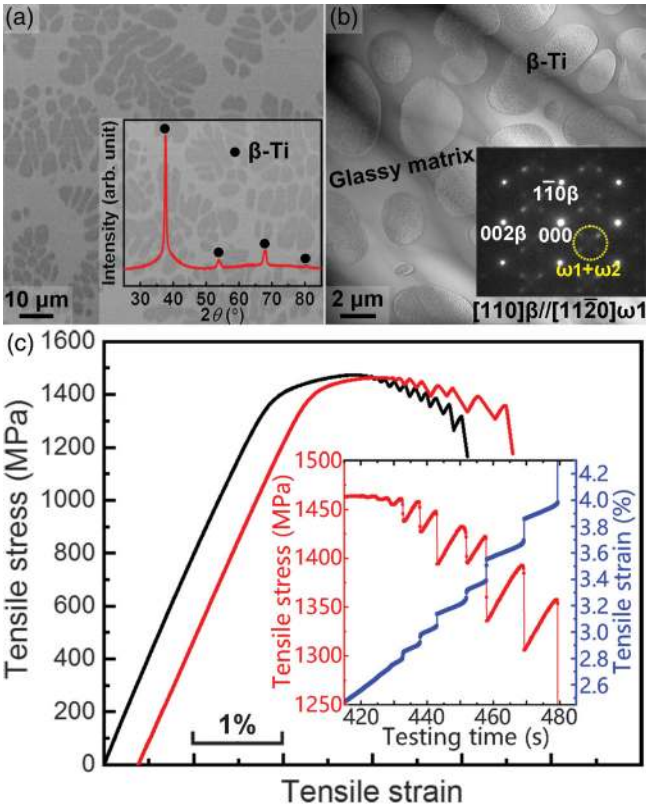

FIG. 1. (a) SEM micrograph and (b) TEM micrograph of the as-cast ϕ14 mm $\mathrm{Ti}_{45.7}\mathrm{Zr}_{33}\mathrm{Cu}_{5.8}\mathrm{Co}_3\mathrm{Be}_{12.5}$ BMGC rod, with insets of the XRD pattern of the BMGC and the SAED pattern from the crystal, respectively. (c) Engineering stress-strain curves under tension with an inset showing the plots of stress and strain vs time.

strain rate of $5 \times 10^{-4}\ \mathrm{s}^{-1}$. A high precision Instron extensometer was firmly attached to the gauge section of each specimen during testing.

The microstructure of the as-cast $\mathrm{Ti}_{45.7}\mathrm{Zr}_{33}\mathrm{Cu}_{5.8}\mathrm{Co}_3\mathrm{Be}_{12.5}$ rods is composed of a dendritic phase distributed homogeneously in a continuous matrix [Fig. 1(a)]. The compositions of the dendrites and the matrix as determined by EDS are $\mathrm{Ti}_{60.6}\mathrm{Zr}_{36.1}\mathrm{Cu}_{2.3}\mathrm{Co}_1$ and $\mathrm{Ti}_{32}\mathrm{Zr}_{30.2}\mathrm{Cu}_9\mathrm{Co}_{4.8}\mathrm{Be}_{24}$, respectively. The average span length of the dendrites is ~50 μm. The average crystal size (size of secondary dendrite arms) and the volume fraction of the crystals are $6.5 \pm 1.2\ \mu$m and $52.5\% \pm 1.5\%$, respectively. The XRD pattern [inset in Fig. 1(a)] shows diffraction peaks from a body-centered cubic (bcc) phase superimposed on the diffraction humps of a glassy phase. The TEM micrograph in Fig. 2(b) reveals that crystals are homogenously embedded in a featureless matrix. The dendritic phase is β-Ti as further confirmed by selected-area electron diffraction (SAED). Athermal ω-Ti forms in the β-Ti dendrites as evident by the weak diffraction spots located at 1/3 or 2/3 $\{\bar{1}1\bar{2}\}_\beta$ positions, and two of four ω-Ti variants can be observed under the zone axis of $[110]_\beta$. The nanometer-sized ω-Ti (see Fig. S1 in the Supplemental Material in Ref. [19]) precipitates via partial collapse of $\{222\}_\beta$ planes [20], suggesting a metastable nature of the β-Ti crystals in the current BMGC.

Two typical tension stress-strain curves of the BMGC are displayed in Fig. 1(c). The BMGC yields at a strength of 1382 ± 18 MPa at a strain of $1.7\% \pm 0.1\%$. After yielding, it plastically deforms accompanying strain hardening until its UTS of 1473 ± 16 MPa at a strain of $2.8\% \pm 0.1\%$. The BMGC further deforms in a serrated manner, and the peak stress of serrations decreases with deformation. The strain burst, known as a shear avalanche, causes a sudden stress

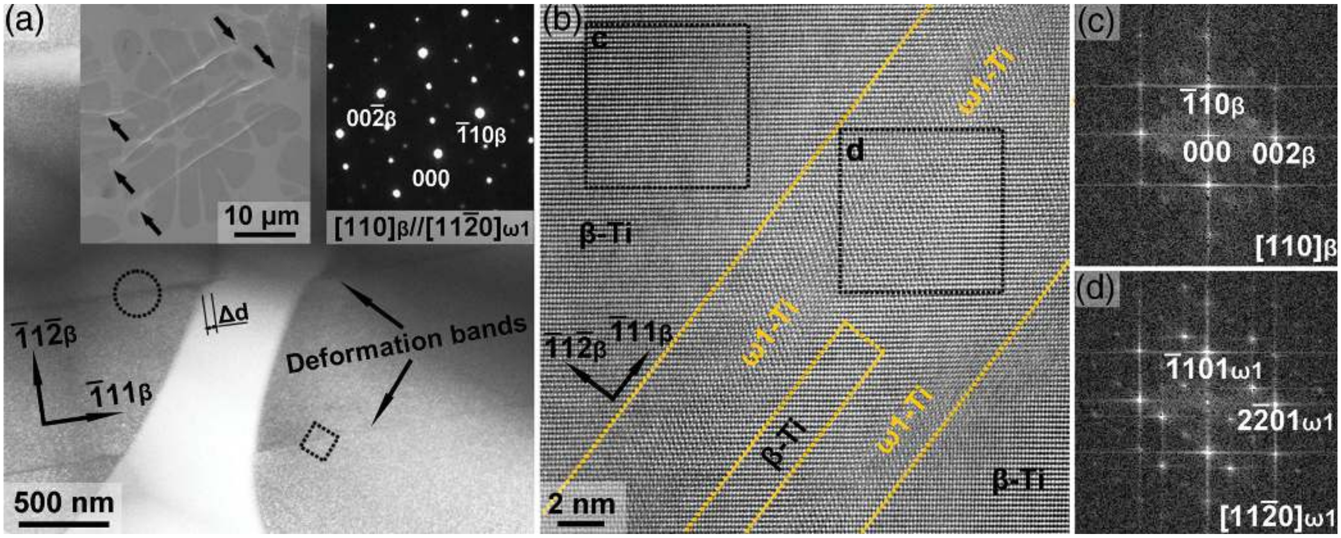

FIG. 2. (a) TEM micrograph and SEM micrograph (left inset) of the tension-fractured $\mathrm{Ti}_{45.7}\mathrm{Zr}_{33}\mathrm{Cu}_{5.8}\mathrm{Co}_3\mathrm{Be}_{12.5}$ BMGC. The right inset in (a) is an SAED pattern from the circle region. (b) HRTEM image from the squared region in (a). (c) and (d) are FFT images from region *c* and region *d*, respectively, in (b).

drop. This process is followed by repeated elastic reloading and shear avalanches [see the inset in Fig. 1(c)]. The BMGC fractures at a tensile strain of $4.1\% \pm 0.2\%$.

The shear avalanches cause a macroscopic shear-fracture plane, having an angle of 53° to the loading direction (see Fig. S2 in Ref. [19]). A typical SEM micrograph from the region close to the shear-fractured plane is shown in the left inset in Fig. 2(a). Local deformation bands penetrating both the glassy matrix and a β-Ti dendrite can be clearly seen, but the deformation bands are impeded by the adjacent β-Ti dendrites, as indicated by arrows. The TEM micrograph [Fig. 2(a)] from the same region clearly shows deformation bands in β-Ti crystals, but the shear bands in the glassy matrix, which connect with the deformation bands in β crystals as observed in SEM, were eliminated during ion-milling of the TEM specimen. The deformation bands are along a $\{\bar{1}1\bar{2}\}\langle\bar{1}11\rangle_\beta$ direction, and the two parts of the β-Ti crystal sheared a distance as large as $\Delta d = 40$ nm along the deformation band, as seen in Fig. 2(a). The SAED pattern [right inset in Fig. 2(a)] from the circle region containing a deformation band shows a similar pattern as for the as-cast state, but the diffraction spots of the ω_1-Ti variant become more intensive. A high-resolution TEM (HRTEM) image obtained from the rectangular region in Fig. 2(a) is shown in Fig. 2(b). The deformation band, as marked by the dotted lines, possesses a different atomic arrangement than the adjacent regions. The fast-Fourier transformed (FFT) image [Fig. 2(c)] of the region c in Fig. 2(b) clearly exhibits β-Ti spots. And the spots located at $1/3\ \{\bar{1}1\bar{2}\}_\beta$ or $2/3\ \{\bar{1}1\bar{2}\}_\beta$ are quite weak. In contrast, the FFT image [Fig. 2(d)] of the region d in the deformation band in Fig. 2(b) only shows spots of the ω_1-Ti variant, suggesting that the β-Ti in the deformation band transforms to ω_1-Ti, possessing a relationship of $(\bar{1}1\bar{2})_\beta \| (\bar{1}100)_{\omega 1}$ and $[\bar{1}11]_\beta \| [0001]_{\omega 1}$. However, a small fraction of β-Ti lattice in the deformation band is still retained, as seen in Fig. 2(b). The thickness of the ω-Ti band is of ~10 nm, similar to the thickness of shear bands in monolithic BMGs [1,2]. This implies a cooperative shear of a shear band in the glassy matrix and an ω-Ti band in the β-Ti dendrite on the scale of tens of micrometers.

Slip avalanches are often encountered in polycrystalline metals arising from interaction between dislocations and solutes known as the PLC effect [21], in nanocrystals via dislocation avalanches [8,22], and in metallic glasses via shear banding [3,4]. Nevertheless, the serrated flow and statistics of slip avalanches in BMGs were merely studied in cases of compression or indentation [3,4,23]. The current BMGC exhibits a unique serrated behavior under tension via the cooperative shear comprising a shear band and an ω-Ti band. Therefore, the statistics of shear avalanches of the BMGC under tension are of scientific interest. The stress drop magnitude $\Delta\sigma$ and the strain burst magnitude $\Delta\varepsilon$ of the serrations in Fig. 1(c) are summarized in Table S1 in Ref. [19]. $\Delta\sigma$ is selected to characterize the sizes of the slip avalanches for statistical analysis [24,25]. The cumulative distribution $P(>\Delta\sigma)$ of the slip sizes follows a power law multiplied by an exponentially decaying function [8,24]:

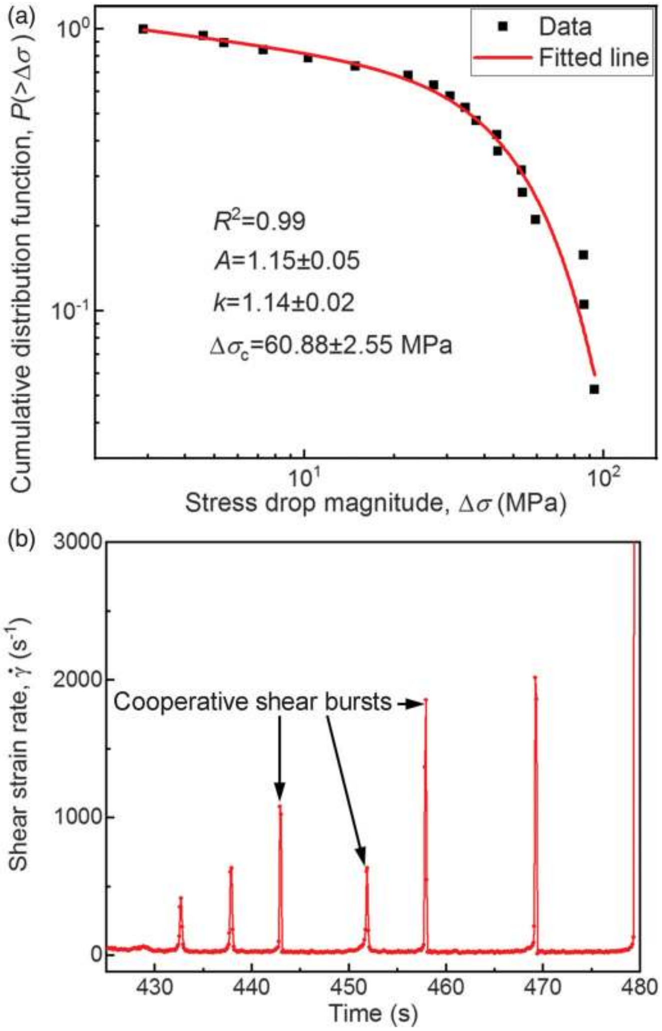

FIG. 3. (a) Plot of the cumulative distribution of stress drops $P(>\Delta\sigma)$ vs stress drop magnitude $\Delta\sigma$. (b) Shear strain rate $\dot{\gamma}$ as a function of time.

$$P(>\Delta\sigma) = A\Delta\sigma^{-(k-1)} \exp[-(\Delta\sigma/\Delta\sigma_C)^2], \qquad (1)$$

where A is a normalized constant, k is a scaling exponent, and $\Delta\sigma_C$ is the cutoff stress drop magnitude. $P(>\Delta\sigma)$ versus $\Delta\sigma$ are plotted in Fig. 3(a), and fitted by Eq. (1). Equation (1) shows a high fitting robustness with $R^2 = 0.99$, and the fitting parameters are $A = 1.15 \pm 0.05$, $k = 1.14 \pm 0.02$, and $\Delta\sigma_C = 60.88 \pm 2.55$ MPa. This implies that the cumulative distribution of shear-avalanche sizes of the BMGC under tension still follows the universal power law multiplied by an exponentially delaying function as predicted by the mean-field interaction model [8,24,26]. Nevertheless, the scaling exponent $k = 1.14$ is smaller than

1.5 in the mean-filed interaction model, which implies a weaker spatial and temporal interaction of shear avalanches and reflects a higher deformation stability of serrated flow [4,27]. Moreover, the cutoff stress drop, $\Delta\sigma_C = 60.88$ MPa, is much higher than that of monolithic BMGs, which are generally less than 20 MPa [24,26]. $\Delta\sigma_C$ acts as the deviation point between the power-law behavior and the exponential decay behavior, which also reflects the stability of serrated plastic deformation. The much higher $\Delta\sigma_C$ of the BMGC than monolithic BMGs suggests a much higher tolerance of the local shear bursts. During the cooperative shear in the BMGC, an entire dendritic region is sheared and the shear strain can be $\Delta d/t \approx 400\%$ ($t \approx 10$ nm is the thickness of shear/ω-Ti bands) or even higher. But the cooperative shear can be efficiently arrested by the adjacent β-Ti dendrites with different crystalline orientations, resulting in a much improved stability of the serrated flow.

Very recently, narrow ω-Ti bands with a thickness of several nanometers were found to form at interfaces during phase transformation of β-Ti to α'-Ti or twinning of metastable β-Ti [28,29]. To our knowledge, mediating plasticity of β-Ti alloys via the formation of ω-Ti bands under quasistatic loading was rarely reported, whereas the formation of ω-Ti under high pressure or shock loading is well known [20,30]. In order to understand the formation of the ω-Ti bands during cooperative shear in the BMGC, the local shear strain rate was analyzed. Considering that a serration arises from a local shear event, Tong *et al.* [27] generated an expression of the local shear strain γ of a shear event:

$$\gamma = \frac{\Delta\varepsilon H}{h\cos\theta}, \tag{2}$$

where $H = 12.5$ mm is the open gauge length of the extensometer, $h \approx 10$ nm is the thickness of the shear bands and ω-Ti bands, and $\theta = 53°$ is the averaged shear angle. Therefore, the local strain rates can be calculated from the strain-time data in the inset in Fig. 1(c):

$$\dot{\gamma} = 2.1 \times 10^6 \times \frac{\partial\Delta\varepsilon}{\partial t}. \tag{3}$$

The plot of $\dot{\gamma}$ versus time is shown in Fig. 3(b). The local strain rates of the strain bursts are on the magnitude of $\sim 10^3$ s^{-1}, about seven magnitude orders higher than the quasistatic tension strain rate. The high local strain rates are comparable to that of shock loading [20,31]. This implies the high local strain rates during the cooperative shear cause the formation of ω-Ti bands in the dendrite with an identical thickness to that of the shear band in the matrix. In addition, the increase of local strain rate [Fig. 3(b)] and meanwhile the almost unchanged flow resistance during deformation also imply the negative strain-rate sensitivity of the resistant flow stress of materials from the mechanical stability analysis [32], which may account for the gradually decreased peak stress of the serrations.

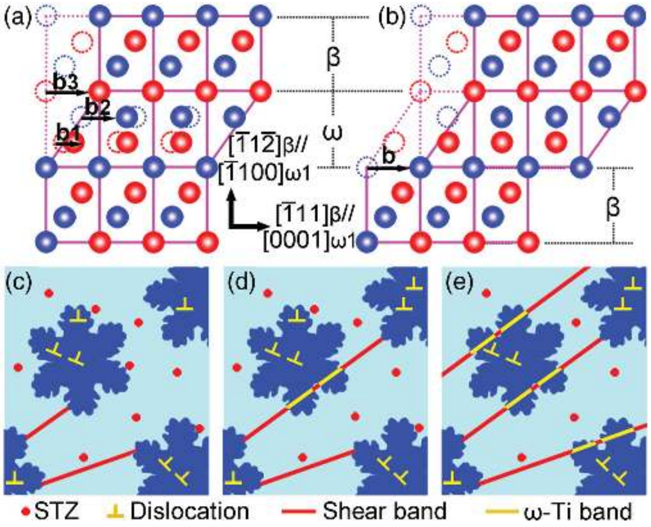

FIG. 4. (a) Transition of β-Ti to ω-Ti via the dissociation of a $\mathbf{b} = 1/2\langle\bar{1}11\rangle_\beta$ dislocation into three partials: $\mathbf{b}_1 = \mathbf{b}_3 = 1/12\langle\bar{1}11\rangle_\beta$ and $\mathbf{b}_2 = 1/3\langle\bar{1}11\rangle_\beta$, gliding on three consecutive $\{\bar{1}1\bar{2}\}_\beta$ planes. (b) Glide of a perfect $\mathbf{b} = 1/2\langle\bar{1}11\rangle_\beta$ dislocation further contributes to the shear strain. (c)–(e) Schematic views of the plastic deformation stages of the $Ti_{45.7}Zr_{33}Cu_{5.8}Co_3Be_{12.5}$ BMGC with increasing tensile strain.

A dislocation dissociation model accounting for the high strain-rate-induced β-Ti to ω-Ti transition has been proposed by Hsiung and Lassila [31]. As seen in Fig. 4(a), a perfect $\mathbf{b} = 1/2\langle\bar{1}11\rangle_\beta$ dislocation dissociates into $\mathbf{b}_1 = \mathbf{b}_3 = 1/12\langle\bar{1}11\rangle_\beta$ and $\mathbf{b}_2 = 1/3\langle\bar{1}11\rangle_\beta$ three partials, which continuously glide on three consecutive $\{\bar{1}1\bar{2}\}_\beta$ planes and result in the $\beta \rightarrow \omega$ transition. This transition is energetically favored due to a lower energy of ω-Ti than metastable β-Ti [28,31]. Also, the retained narrow β-Ti strip parallel to the $[\bar{1}11]_\beta \| [0001]_\omega$ direction in Fig. 2(b) is an evidence of this dislocation dissociation model. However, the strain accompanying this transition is only

$$\gamma = \frac{|\mathbf{b}|}{3d_{\{\bar{1}1\bar{2}\}\beta}} = \frac{\sqrt{3}a_\beta/2}{\sqrt{6}a_\beta/2} \approx 70.7\%, \tag{4}$$

where $d_{\{\bar{1}1\bar{2}\}\beta}$ is the interplanar distance of $\{\bar{1}1\bar{2}\}_\beta$ planes. This strain is much smaller than the observed strain of the cooperative shear in the BMGC. In fact, as cooperative shear causes the formation of an ω-Ti band, the connected shear bands in the glassy matrix dilate and are softened, and further deformation strains are prone to being localized in this band. Consequently, many $\mathbf{b} = 1/2\langle\bar{1}11\rangle_\beta$ dislocations are activated. Because of the coherent nature of $\{\bar{1}1\bar{2}\}_\beta \| \{\bar{1}100\}_\omega$ interfacial planes between β and ω, the $\{\bar{1}1\bar{2}\}\langle\bar{1}11\rangle_\beta$ perfect dislocations can correspondingly transfer to $\{\bar{1}100\}\langle 0001\rangle_\omega$ dislocations as entering the ω domains [30,31]. The glide of $\{\bar{1}1\bar{2}\}\langle\bar{1}11\rangle_\beta$ or $\{\bar{1}100\}\langle 0001\rangle_\omega$ perfect dislocations, as depicted in Fig. 4(b), further contributes to the observed large shear strains.

The mechanisms of plastic deformation of the $Ti_{45.7}Zr_{33}Cu_{5.8}Co_3Be_{12.5}$ BMGC are schematically presented in Figs. 4(c)–4(e). The interfacial stress concentration first causes the yielding of β-Ti crystals via nucleation and gliding of dislocations [33], which causes the glassy matrix to bear a higher stress. The high stress concentration at interface then activates STZs in the glassy matrix, which are percolated to form a shear band [34,35], resulting in the macroscopic yielding of the BMGC. After yielding, the shear bands in the glassy matrix are well restricted in the intercrystalline glassy regions [12,36], as depicted in Fig. 4(c) and seen in Fig. S3 in Ref. [19]. Upon further deformation, an ω-Ti deformation band forms in the metastable β-Ti dendrite, which has a $\{\bar{1}1\bar{2}\}\langle\bar{1}11\rangle_\beta$ direction close to the shear direction. Strains are transferred from one side to another side of the dendrite accompanying a high local strain rate, and new shear bands form in the glassy matrix, resulting a cooperative shear on the scale of tens of micrometers [see Fig. 4(d)]. However, the local cooperative shear is impeded by the adjacent β-Ti dendrites with different crystalline orientations, because the different orientations require a much higher critical stress for gliding of dislocations [37]. Then, other cooperative shear events are activated in further deformation, as shown in Fig. 4(e), leading to serrations on the stress-strain curves. The thickness of ω-Ti bands is ~10 nm [see Fig. 2(b)], which substantiates that the core thickness of shear bands is also ~10 nm due to the continuous transfer of plastic strains between both bands. It is obvious that the occurrence of the cooperative shear events is mainly associated with the metastability of the β-Ti phase. BMGCs containing larger-sized or higher fraction of metastable β-Ti dendrites also exhibit a similar serrated manner (Figs. S4 and S5 in Ref. [19]). Actually, the current cooperative shear mechanism is of a wide universality, which also accounts for the previously observed serrated flow in BMGCs containing metastable β-Ti in other alloy systems [38,39].

In conclusion, a novel plastic deformation mechanism of BMGCs containing metastable β-Ti dendrites under tension has been uncovered. The plastic deformation of the BMGCs beyond the UTS is governed by the cooperative shear events, which comprise a shear band in the glassy matrix and a continuous ω-Ti band in the β-Ti dendrite. The formation of ω-Ti bands with a thickness of ~10 nm is caused by a high local strain rate, which substantiates that the intrinsic thickness of shear bands is also ~10 nm. Cooperative shear causes serrations and results in a macroscopic shear fracture. The cumulative distribution of the shear-avalanche sizes of the BMGC under tension still follows the universal scaling function as depicted by the mean-field theory with a low scaling exponent and a high cutoff stress drop magnitude, both of which reflect a high stability of the serrated flow.

This work was supported by the National Key Research and Development Program of China (2018YFB0703402), the National Natural Science Foundation of China (No. 51701213, No. 51790484, and No. 51822107), the Liaoning Revitalization Talents Program (XLYC1802078), Chinese Academy of Sciences (ZDBS-LY-JSC023), the European Research Council (ERC) under the ERC Advanced Grant INTELHYB (Grant No. ERC-2013-ADG-340025), and the Ji Hua Laboratory in Foshan, China.

---

[*] Corresponding author.
hfzhang@imr.ac.cn

[1] A. L. Greer, Y. Q. Cheng, and E. Ma, Mater. Sci. Eng. R **74**, 71 (2013).

[2] C. Schuh, T. Hufnagel, and U. Ramamurty, Acta Mater. **55**, 4067 (2007).

[3] B. A. Sun, S. Pauly, J. Hu, W. H. Wang, U. Kühn, and J. Eckert, Phys. Rev. Lett. **110**, 225501 (2013).

[4] J. Antonaglia, W. J. Wright, X. Gu, R. R. Byer, T. C. Hufnagel, M. LeBlanc, J. T. Uhl, and K. A. Dahmen, Phys. Rev. Lett. **112**, 155501 (2014).

[5] M. D. Demetriou, J. S. Harmon, M. Tao, G. Duan, K. Samwer, and W. L. Johnson, Phys. Rev. Lett. **97**, 065502 (2006).

[6] G. Wang, K. C. Chan, L. Xia, P. Yu, J. Shen, and W. H. Wang, Acta Mater. **57**, 6146 (2009).

[7] D. Klaumünzer, R. Maaß, and J. F. Löffler, J. Mater. Res. **26**, 1453 (2011).

[8] F. F. Csikor, C. Motz, D. Weygand, M. Zaiser, and S. Zapperi, Science **318**, 251 (2007).

[9] S. Pauly, S. Gorantla, G. Wang, U. Kühn, and J. Eckert, Nat. Mater. **9**, 473 (2010).

[10] C. C. Hays, C. P. Kim, and W. L. Johnson, Phys. Rev. Lett. **84**, 2901 (2000).

[11] D. C. Hofmann, J. Y. Suh, A. Wiest, G. Duan, M. L. Lind, M. D. Demetriou, and W. L. Johnson, Nature (London) **451**, 1085 (2008).

[12] J. W. Qiao, A. C. Sun, E. W. Huang, Y. Zhang, P. K. Liaw, and C. P. Chuang, Acta Mater. **59**, 4126 (2011).

[13] L. Zhang, R. L. Narayan, H. M. Fu, U. Ramamurty, W. R. Li, Y. D. Li, and H. F. Zhang, Acta Mater. **168**, 24 (2019).

[14] Y. Wu, Y. H. Xiao, G. L. Chen, C. T. Liu, and Z. P. Lu, Adv. Mater. **22**, 2770 (2010).

[15] J. Eckert, J. Das, S. Pauly, and C. Duhamel, J. Mater. Res. **22**, 285 (2006).

[16] H. C. Sun, Z. L. Ning, J. L. Ren, W. Z. Liang, Y. J. Huang, J. F. Sun, X. Xue, and G. Wang, J. Mater. Sci. Technol. (Sofia) **35**, 2079 (2019).

[17] Y. S. Oh, C. P. Kim, S. Lee, and N. J. Kim, Acta Mater. **59**, 7277 (2011).

[18] Standard Test Methods for Tension Testing of Metallic Materials, in *Annual Book of ASTM Standards* Vol. 3.01

(ASTM International, West Conshohocken, PA, 2011), p. 130, https://www.astm.org/BOOKSTORE/BOS/0301.htm.

[19] See Supplemental Material athttp://link.aps.org/supplemental/10.1103/PhysRevLett.125.055501 for Figs. S1–S5 and Table S1.

[20] S. Banerjee, R. Tewari, and G. K. Dey, Int. J. Mat. Res. **97**, 963 (2006).

[21] M. A. Lebyodkin, Y. Brechet, Y. Estrin, and L. P. Kubin, Phys. Rev. Lett. **74**, 4758 (1995).

[22] N. Friedman, A. T. Jennings, G. Tsekenis, J.-Y. Kim, M. Tao, J. T. Uhl, J. R. Greer, and K. A. Dahmen, Phys. Rev. Lett. **109**, 095507 (2012).

[23] C. A. Schuh, A. C. Lund, and T. G. Nieh, Acta Mater. **52**, 5879 (2004).

[24] B. A. Sun, S. Pauly, J. Tan, M. Stoica, W. H. Wang, U. Kühn, and J. Eckert, Acta Mater. **60**, 4160 (2012).

[25] W. J. Wright, A. A. Long, X. Gu, X. Liu, T. C. Hufnagel, and K. A. Dahmen, J. Appl. Phys. **124**, 185101 (2018).

[26] W. J. Wright, Y. Liu, X. Gu, K. D. V. Ness, S. L. Robare, X. Liu, J. Antonaglia, M. LeBlanc, J. T. Uhl, T. C. Hufnagel, and K. A. Dahmen, J. Appl. Phys. **119**, 084908 (2016).

[27] X. Tong, G. Wang, J. Yi, J. L. Ren, S. Pauly, Y. L. Gao, Q. J. Zhai, N. Mattern, K. A. Dahmen, P. K. Liaw, and J. Eckert, Int. J. Plast. **77**, 141 (2016).

[28] M. J. Lai, C. C. Tasan, J. Zhang, B. Grabowski, L. F. Huang, and D. Raabe, Acta Mater. **92**, 55 (2015).

[29] P. Castany, Y. Yang, E. Bertrand, and T. Gloriant, Phys. Rev. Lett. **117**, 245501 (2016).

[30] M. J. Lai, T. Li, and D. Raabe, Acta Mater. **151**, 67 (2018).

[31] L. M. Hsiung and D. H. Lassila, Acta Mater. **48**, 4851 (2000).

[32] J. R. Rice and A. L. Ruina, J. Appl. Mech. **50**, 343 (1983).

[33] Y. Cui, Y. Shibutani, S. Li, P. Huang, and F. Wang, J. Alloys Compd. **693**, 285 (2017).

[34] A. S. Argon, Acta Metall. **27**, 47 (1979).

[35] B. Xu, M. L. Falk, J. F. Li, and L. T. Kong, Phys. Rev. Lett. **120**, 125503 (2018).

[36] D. Şopu, A. Stukowski, M. Stoica, and S. Scudino, Phys. Rev. Lett. **119**, 195503 (2017).

[37] Y. Cui, Y. Shibutani, P. Huang, F. Wang, K. Xu, and T. Lu, Mater. Trans., JIM **59**, 230 (2018).

[38] J. A. Kolodziejska, H. Kozachkov, K. Kranjc, A. Hunter, E. Marquis, W. L. Johnson, K. M. Flores, and D. C. Hofmann, Sci. Rep. **6**, 22563 (2016).

[39] D. Liu, Z. Zhu, Z. Li, L. Zhang, H. Fu, A. Wang, H. Li, H. Zhang, Y. Wang, and H. Zhang, Scr. Mater. **146**, 22 (2018).